Second-order imaginary differential operator for effective absorption in the numerical solution of the time-dependent Schrödinger equation

A. A. Silaev [1,2,*] A. A. Romanov [1,2] M. V. Silaeva [3] and N. V. Vvedenskii [1,2]

[1]*Institute of Applied Physics, Russian Academy of Sciences, Nizhny Novgorod 603950, Russia*

[2]*Department of Radiophysics, University of Nizhny Novgorod, Nizhny Novgorod 603950, Russia*

[3]*HSE University, Nizhny Novgorod 603155, Russia*

(Received 30 March 2023; revised 7 June 2023; accepted 30 June 2023; published 27 July 2023)

We propose a method to implement absorbing layers for the numerical solution of the time-dependent Schrödinger equation (TDSE) in the open domain. The method is based on introducing an imaginary second-order differential operator which effectively absorbs waves propagating both toward the boundary and away from it. The survival probability is 0.01 for de Broglie wavelength equal to the layer width and decreases exponentially as the wavelength decreases. The proposed method can be used in both length and velocity gauges for the electric field when solving strong-field physics problems. We also propose the propagator for the absorbing operator for convenient use in the Fourier split-step method of the TDSE solution. We demonstrate the high accuracy of using the proposed method in simulations of the high-order harmonics generation in atomic hydrogen by femtosecond laser pulses and calculations of photoelectron momentum distributions using projections of the absorbed wave packets onto Volkov states.

DOI: 10.1103/PhysRevA.108.013118

I. INTRODUCTION

The time-dependent Schrödinger equation (TDSE) is one of the main tools to study various physical phenomena in strong-field physics, as well as in several other areas, which include nonlinear optics, plasma physics, condensed matter physics, and others. When studying various phenomena in strong fields, the TDSE can be used as a stand-alone tool or be an integral part of approximate many-electron approaches such as the time-dependent Kohn-Sham equations (TDKSE). In the mathematical formulation of many problems based on TDSE (for example, when considering the interaction of atoms and molecules with laser fields), the considered domain is open, i.e., boundaries are at infinity. However, the computational domain always has a finite size when performing numerical simulations using grid methods. Therefore, absorbing layers are used that suppress unphysical waves appearing near computational grid boundaries due to wave packets' reflection (and wrap-around when using numerical periodic boundary conditions) [1–9].

During simulations of strong-field phenomena within the TDSE, efficient absorption in a wide range of de Broglie wavelengths is often of fundamental importance. When an atom or molecule interacts with an ionizing infrared (IR) laser pulse, the freed electrons can be accelerated up to high energies. Due to rescattering, photoelectrons can gain energy close to $\sim 10U_p$, where U_p is the electron ponderomotive energy [10–14]. Therefore, the wave function has a very broad spatial spectrum. In the case of insufficient absorption in some wavelength ranges, the artifact wave packets that appear near boundaries can lead to incorrect calculation of the high-energy part of photoelectron momentum distribution (PMD) or low-energy structures in PMD, which currently attract much attention [13,15–19]. It should be noted that the need for effective absorption is present in all methods of PMD calculation, including the time-dependent surface flux (t-SURFF) method [13,19–23]. Inefficient absorption can also strongly affect the excited low-frequency currents that determine the secondary generated radiation in terahertz and mid-IR ranges [24–32]. Finally, efficient absorption is important in the numerical simulations of high-order harmonics generation (HHG) of a laser pulse by atoms and molecules caused by the ionization and acceleration of electrons by the laser field and their recombination with parent ions [2,33–36]. This becomes especially important when studying harmonics with small yield, which appear, for example, beyond the cutoff of the plateau in the HHG spectrum when extreme-ultraviolet (XUV) pulse is added to the driving IR field [37–41].

The currently used methods for implementing absorbing layers include exterior complex scaling (ECS), in which a linear scaling transformation of the coordinate outside a certain region is performed so that outgoing waves fall off with increasing coordinate [1,3,4,22,42]. Although ECS can provide a wide absorption range and does not distort the wave-function behavior in the inner region (out of the absorbing layer), this method has essential disadvantages. First, the application of the Fourier split-step method along with ECS is impeded by the explicit coordinate dependence of the scaled kinetic energy operator [43]. Second, when describing the interaction with an external field, the ECS method works only in the velocity gauge (VG) and fails in the length gauge (LG) [1,3]. Another absorption method called "perfectly matched layers" (PMLs)

*silaev@appl.sci-nnov.ru

is based on replacing the kinetic energy operator with the operator $-\frac{1}{2}c(x)[\frac{\partial}{\partial x}c(x)\frac{\partial\psi}{\partial x}]$, where ψ is the wave function; $c(x) = 1/[1 + e^{i\gamma}\sigma(x)]$; $\sigma(x)$ is a real, non-negative function, which is zero outside the layer; and $0 < \gamma < \pi/2$ to ensure decay of the wave packet as it travels out of the interior domain [5,9,44]. PMLs effectively absorb freely propagating wave packets but lead to large errors when solving TDSE in the LG; in the VG, the errors appear if the ion potential reaches into the absorbing domain [9]. In addition, there is no proposed propagator to implement PMLs in the Fourier split-step method. In this regard, the PMLs are currently not used in simulations of strong-field phenomena.

The most commonly used absorption method is based on complex absorbing potentials (CAPs) [13,45–51]. CAPs can be used for different grid-based algorithms for solving TDSE in both LG and VG for the electric field [52,53]. In particular, purely imaginary CAPs are used in open-source codes for solving three-dimensional (3D) TDSE QPROP [19,54] SCID-TDSE [55], CLTDSE [56], and QPC-TDSE [23] that use the expansion of wave function in spherical harmonics, as well as codes PCTDSE [57] and OCTOPUS [58,59] developed in Cartesian coordinates (codes QPROP and OCTOPUS can also solve TDKSE). The use of negative imaginary potential is equivalent to multiplying the wave function by a mask function less than unity with some small time step [2,42]. The parts of the wave function that pass into regions with imaginary potential are absorbed and do not appear later on the grid but can be projected onto Volkov states. The sum of these projections gives the residual wave function in momentum space, the square of which is PMD [48,60]. The latter is widely used to calculate PMD for both single-electron and multielectron systems [14,57,61–63]. However, the range of de Broglie wavelengths effectively absorbed by CAP is finite and strongly depends on the shape and amplitude of the potential [2,35,64,65]. Effective absorption in a wide range requires a wide layer and a specially selected potential shape, dependent on the parameters of the physical problem. In our recent work [65], we proposed to use CAPs containing several imaginary humps with different widths and amplitudes that absorb different waves. This method can provide the required absorption level in a given finite wavelength range, whose upper limit equals the layer width. However, the parameters of the imaginary humps and their number need to be carefully defined based on the physical problem being solved. In this regard, the development of simple, universal, and efficient absorption methods is still a topical problem.

In this paper, we develop an absorption method based on a second-order imaginary differential operator with a smooth bell-shaped envelope. The second derivative of the wave function multiplied by a properly chosen constant corresponds to the optimal damping rate, which is a quadratic function of the wave number. The resulting survival probability decreases exponentially with decreasing de Broglie wavelength. We propose an algorithm for the efficient implementation of this method using the Fourier split-step technique of the TDSE solution for both LG and VG. The effectiveness of the absorption algorithm is demonstrated in calculating HHG spectra in a two-color field consisting of IR and XUV components and in calculating PMD in the IR field based on the projections of absorbed wave packets onto Volkov states. In addition, we find a way to eliminate the unphysical circles structure in PMDs seen in many published numerical results (see, e.g., Fig. 1(a) in Ref. [12] or Fig. 1 in Ref. [66]).

The article is organized as follows. In Sec. II, we construct an imaginary absorbing operator, examine its absorbing properties, and adapt it for convenient use in the Fourier split-step method. In Sec. III, we demonstrate the developed absorption method performance in calculating HHG spectra of a hydrogen atom in a two-color IR and XUV pulse, as well as the calculation of PMD in a hydrogen atom under the action of a short IR pulse based on the 3D TDSE solution in Cartesian coordinates. Section IV concludes the research. Atomic units (a.u.) are used throughout this paper unless noted otherwise.

II. CONSTRUCTION OF IMAGINARY DIFFERENTIAL ABSORBING OPERATOR

The construction of the complex differential operator is based on absorption properties of bell-shaped imaginary potentials [65]. Let us consider the one-dimensional (1D) stationary Schrödinger equation (SSE)

$$-\frac{1}{2}\frac{d^2\psi}{dx^2} + V_{\text{imag}}(x)\psi = \frac{k^2}{2}\psi \tag{1}$$

with the boundary conditions corresponding to a plane wave incident from the left with a wave number k:

$$\psi(x) = \begin{cases} e^{ikx} + \tilde{r}e^{-ikx}, & x \to -\infty, \\ \tilde{t}e^{ikx}, & x \to \infty, \end{cases} \tag{2}$$

where it is supposed that the potential $V_{\text{imag}}(x)$ tends to zero at infinity. We consider single-hump imaginary potentials of the Gaussian shape [65]:

$$V_{\text{imag}}(x) = -iuf[(x - x_c)/l], \quad f(\xi) = e^{-(4\ln 2)\xi^2}. \tag{3}$$

Here, $f(\xi)$ is a smooth bell-shaped function such that $f(0) = 1$, $f(1/2) = 1/2$, l is the width of the potential at the level $1/2$, and x_c is the potential center. Both the amplitude u and the width l of the potential are positive quantities that determine the transmission and reflection coefficients, $T = |\tilde{t}|^2$ and $R = |\tilde{r}|^2$, respectively. The sum of these coefficients, $S = R + T$, is called survival probability, and $S \leqslant 1$ due to the wave function outflow in the imaginary potential region. The less the survival probability, the higher the absorption efficiency.

For a fixed width of the single-hump potential, there is an optimal amplitude at which the survival probability for a given wave number k is minimal. The optimal amplitude $u = u_{\text{opt}}$ of potential (3) found from numerical calculations in the range of wave numbers $kl \sim 1 - 10$ is well approximated by the quadratic function [65]

$$u_{\text{opt}} = \varepsilon_{\text{opt}}(kl)/l^2, \quad \varepsilon_{\text{opt}}(\kappa) = C + D\kappa^2, \quad C = 2.2, \quad D = 0.9.$$

When the amplitude is lower or higher than u_{opt}, the survival probability is higher due to the transmission or reflection coefficient increase. Similarly, for a given amplitude u and width l, there is an optimal wave number below or above which the survival probability is higher due to an increase in the reflection or transmission coefficient; as a result, the range

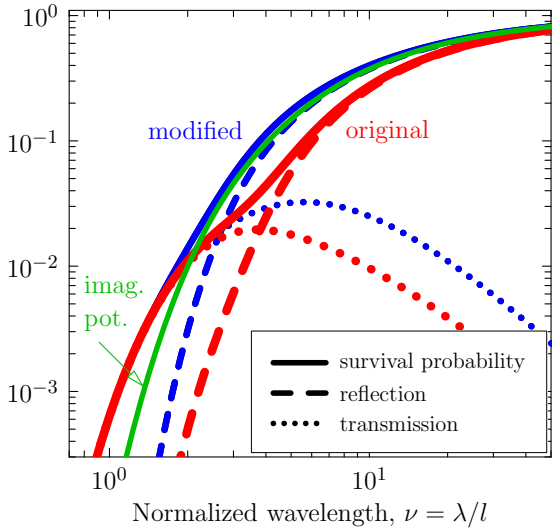

FIG. 1. The dependences of reflection (R) and transmission (T) coefficients and survival probability $S = R + T$ on the normalized wavelength $\nu = \lambda/l$ for two imaginary differential operators: original [Eq. (4), thick red lines] and modified [Eq. (16), thin blue lines]. The green thin solid line denotes the wavelength dependence of the minimal survival probability $S_{\min}$ (corresponding to the optimal amplitude u_{opt} for a given wavelength) provided by imaginary potential (3).

of de Broglie wavelengths $\lambda = 2\pi/k$ corresponding to effective absorption is limited. The minimum survival probability $S_{\min} = S(u_{\text{opt}})$ corresponding to the optimal amplitude u_{opt} decreases exponentially with decreasing λ, which is demonstrated in Fig. 1 (see Appendix A for details of calculations).

The quadratic dependence of the optimal amplitude of potential on the wave number allows us to construct a second-order complex differential operator with optimal absorption for different de Broglie wavelengths. For a sufficiently smooth function f, multiplying the plane wave e^{ikx} by $k^2 f$ is equivalent to applying the second derivative to $-fe^{ikx}$. Thus, we propose to use a complex absorbing operator of the form

$$\hat{V}_{\text{abs}}\psi = -i\frac{C}{l^2}f\psi + iD\frac{\partial}{\partial x}\left(f\frac{\partial\psi}{\partial x}\right). \tag{4}$$

When an operator (4) is used in the TDSE, the norm of the wave function in the absorbing layer strictly decreases with time for an arbitrary wave function. To show this, let us consider 1D TDSE with an absorbing operator $\hat{V}_{\text{abs}}$,

$$i\frac{\partial\psi}{\partial t} = \hat{H}\psi + \hat{V}_{\text{abs}}\psi, \quad \hat{H} = -\frac{1}{2}\frac{\partial^2}{\partial x^2} + V(x,t), \tag{5}$$

where $V(x,t)$ is the time-dependent potential. The TDSE (5) with $V(x,t) = V_c(x) + xE(t)$ describes the evolution of the electron wave function ψ in the core potential $V_c(x)$ under the action of the electric field $E(t)$ in the LG assuming that electron charge is $e = -1$. Multiplying (5) by the complex conjugate wave function, subtracting the complex conjugate equation, and integrating over x gives the time derivative of the norm $N(t) = \int |\psi|^2 dx$:

$$\frac{dN}{dt} = \gamma, \quad \gamma = -\frac{2C}{l^2}\int f|\psi|^2 dx - 2D\int f\left|\frac{\partial\psi}{\partial x}\right|^2 dx. \tag{6}$$

Since the integrands are positive, the norm of the wave function is a monotonically decreasing function of time. Also, absorption is equally efficient for waves propagating in positive and negative directions.

To implement the proposed method in the TDSE solution, one should introduce the absorbing operator near the boundaries of the computational grid. The Gaussian function (3) used to define the shape of the envelope of the absorbing differential operator is nonzero for any arguments but decays rapidly; as a result, the effective absorption occurs in the layers with sizes $2l$ near the grid boundaries.

In order to study the absorbing properties of the constructed operator (4), we solve the 1D SSE

$$-\frac{1}{2}\frac{d^2\psi}{dx^2} + \hat{V}_{\text{abs}}\psi = \frac{k^2}{2}\psi, \tag{7}$$

with boundary conditions (2). The details of numerical calculations can be found in Appendix A. Figure 1 shows the survival probability and reflection and transmission coefficients as functions of the normalized wavelength $\nu = \lambda/l$. The survival probability is exponentially small for $\nu \ll 1$ and increases monotonically with ν, similar to the dependence $S_{\min}(\nu)$ for the single-hump imaginary potential. However, the survival probability for operator (4) is smaller than $S_{\min}(\nu)$ for $\nu > 2$, which means that the absorbing operator is even more effective than imaginary potential with optimal wavelength-dependent amplitude. For $\nu = 4$, the difference is three times, approximately. For $\nu < 2$, the obtained survival probability is slightly higher than $S_{\min}(\nu)$, with a difference increasing towards smaller ν. In this range, the reflection is much less than the transmission, while for $\nu > 4$, on the contrary, the survival probability is determined mainly by the reflection from the layer. In particular, $S(\nu)$ takes the values $S(1) \approx 6 \times 10^{-4}$, $S(2) \approx 0.01$, $S(10) \approx 0.3$. At $\nu \to \infty$, $S(\nu)$ asymptotically tends to unity.

A. Implementation in the Fourier split-step method

The proposed imaginary absorbing operator (4) can be used both in finite difference methods [46,54,58,59] and the Fourier split-step method [25,57,66,67] of TDSE solving. Let us consider the last one with regard to 1D TDSE (5). The corresponding second-order propagator over the time step Δt is [67]

$$\psi(x, t+\Delta t) = e^{-i\hat{V}_{\text{abs}}\Delta t/2}\hat{U}_H e^{-i\hat{V}_{\text{abs}}\Delta t/2}\psi(x,t) + O[(\Delta t)^3] \tag{8}$$

$$\hat{U}_H = e^{-iV(x,\bar{t})\Delta t/2}e^{-i\hat{p}^2\Delta t/2}e^{-iV(x,\bar{t})\Delta t/2}, \tag{9}$$

where $\bar{t} = t + \Delta t/2$, $\hat{U}_H$ is the propagator of the Hamiltonian $\hat{H}$ and $\hat{p} = -i(\partial/\partial x)$ is the momentum operator. The time-evolution operator $e^{-i\hat{V}_{\text{abs}}\Delta t/2}$ responsible for absorption cannot be expressed as a product of operator exponents which could be applied exactly in coordinate or momentum space, i.e., $\hat{V}_{\text{abs}}$ is not separable. To show this, let us rewrite (4) as

$$\hat{V}_{\text{abs}}\psi = -i\left(\frac{C}{l^2} + D\hat{p}^2\right)[f\psi] + D\hat{p}\left[\frac{df}{dx}\psi\right]. \tag{10}$$

Here, the momentum operator acts on $f\psi$ and $(df/dx)\psi$, but not on ψ as the kinetic energy operator in the Hamiltonian.

Consider the absorbing propagator over some small time step $\Delta t_{\rm abs}$:

$$\hat{U}_{\rm abs} = e^{-i\hat{V}_{\rm abs}\Delta t_{\rm abs}}. \tag{11}$$

The first-order expansion of $\hat{U}_{\rm abs}$ in $\Delta t_{\rm abs}$ is

$$\hat{U}_{\rm abs}\psi \approx (1 - i\Delta t_{\rm abs}\hat{V}_{\rm abs})\psi \tag{12}$$

$$= \psi + \hat{\mathcal{F}}^{-1}\left[B_1(p)\hat{\mathcal{F}}[f\psi] + B_2(p)\hat{\mathcal{F}}\left[\frac{df}{dx}\psi\right]\right], \tag{13}$$

$$B_1(p) = -(C/l^2 + Dp^2)\Delta t_{\rm abs}, \quad B_2(p) = -iDp\Delta t_{\rm abs}, \tag{14}$$

where $\hat{\mathcal{F}}[\psi] = \int_{-\infty}^{\infty}\psi e^{-ipx}dx$ and $\hat{\mathcal{F}}^{-1}[\cdot]$ are the forward and backward Fourier transforms, respectively. The use of this approximation applied to $e^{-i\hat{V}_{\rm abs}\Delta t/2}$ in propagator (8) makes the numerical scheme for TDSE solving unstable due to the growth of $|B_1(p)|$ and $|B_2(p)|$ with increasing $|p|$. To improve the accuracy, one can try to use the second-order propagator (for example, using the method suggested in Ref. [68]), but this is associated with the need to calculate several additional fast Fourier transforms (FFTs) along with three FFTs in the case of (13). We suggest to replace $B_1(p)$ in (13) by its exponent form and neglect the second term:

$$B_1(p) = e^{-(C/l^2+Dp^2)\Delta t_{\rm abs}} - 1, \quad B_2(p) = 0. \tag{15}$$

The first term in the expansion of $B_1(p)$ from (15) in $\Delta t_{\rm abs}$ gives $B_1(p)$ from (14). Propagator (13) with (15) requires only two FFTs and makes the numerical scheme stable for an arbitrarily large time step due to the limitation of $|B_1(p)|$ growth with increasing $|p|$. Also, this propagator retains the high absorbing properties of the original absorbing operator (4). To show this, first note that for the waves with squared momenta $p^2 \ll (D\Delta t_{\rm abs})^{-1}$, the action of propagator (13) with (15) corresponds to an absorbing operator

$$\hat{V}_{\rm abs}\psi = -i\left(\frac{C}{l^2} + D\hat{p}^2\right)[f\psi], \tag{16}$$

which is the same as (10) but without the last term containing $\hat{p}[(df/dx)\psi]$. Note that as $|p|$ grows, $B_1(p)$ tends to -1, which means that for rapidly moving wave packets with $p^2 \gg (D\Delta t_{\rm abs})^{-1}$, the action of $\hat{U}_{\rm abs}$ is equivalent to multiplying the wave function by the mask function $M(x) = 1 - f(x)$ equal to zero at the center of the layer and unity outside the layer. At the same time, wave packets with $p^2 \lesssim (D\Delta t_{\rm abs})^{-1}$ are absorbed more weakly with the rate defined by $|B_1(p)|$.

Let us now study the absorbing properties of the modified absorbing operator (16). The derivative of the norm of the wave function when solving the TDSE (5) using the operator (16) contains an extra term with df/dx in the integrand:

$$\frac{dN}{dt} = \gamma - D\int\frac{df}{dx}\frac{\partial|\psi|^2}{\partial x}dx, \tag{17}$$

where γ is taken from (6). When considering a plane wave incident from the left, we have $\partial|\psi|^2/\partial x < 0$, and df/dx takes positive values in the left half of the absorbing layer; then, the extra term is positive. Thus, the absorption should be less effective compared to the original operator (4) [or (10)]. However, the decrease in absorption is pronounced in a narrow wavelength range. Figure 1 shows the survival probability and reflection and transmission coefficients found based on solving the SSE (7) with operator (16) and boundary conditions (2) (see Appendix A for details). For $\nu < 2$, the reflection coefficient (and, accordingly, the survival probability) practically does not change compared with the original operator (4). For $\nu > 2$, the survival probability $S(\nu)$ is higher compared to the original operator and very close to the dependence $S_{\min}(\nu)$ obtained for the single-hump imaginary potential. Thus, the efficiency of absorption of the modified operator corresponds to the efficiency of the imaginary potential with the optimal amplitude.

Since the absorbing propagator (13) with (15) provides numerical scheme stability for arbitrary time step, it is not necessary to apply two time-evolution operators $\hat{U}_{\rm abs}$ every time step Δt in the Fourier split-step method. One can make the step $\Delta t_{\rm abs}$ in the $\hat{U}_{\rm abs}$ propagator many times larger than the main Hamiltonian propagator step Δt. Since the absorbing propagator is time independent, the upper constraint on the time step $\Delta t_{\rm abs}$ is the impossibility of waves passing through the layer in the interval $\Delta t_{\rm abs}$, i.e., $\Delta t_{\rm abs} \ll l/p_0$ [60]. When $\Delta t_{\rm abs} = n\Delta t$, the absorption is performed once every n times, and the total propagator is

$$\psi(x, t + \Delta t_{\rm abs}) = \hat{U}_{\rm abs}\left[\mathcal{T}\left(\prod_{j=1}^{n}\hat{U}_j\right)\psi(x, t)\right], \tag{18}$$

where $\mathcal{T}$ is time ordering operator and $\hat{U}_j$ is the Hamiltonian propagator from $t + (j-1)\Delta t$ to $t + j\Delta t$:

$$\hat{U}_j\psi = e^{-iV(x,\bar{t}_j)\Delta t/2}\hat{\mathcal{F}}^{-1}[e^{-ip^2\Delta t/2}\hat{\mathcal{F}}[e^{-iV(x,\bar{t}_j)\Delta t/2}\psi]],$$

where $\bar{t}_j = t + (j - 1/2)\Delta t$. As a result, applying the propagator $\hat{U}_{\rm abs}$ does not decrease the computer program performance.

It should be noted that earlier in the paper [35], an absorption algorithm was proposed for the Fourier split-step method based on the same propagator as (13), (15) but with a different wave absorption rate, corresponding to $B_1(p) = \exp(-\beta|p|\Delta t_{\rm abs}) - 1$, where β is a constant. The resulting survival probability tends to some constant dependent on β as the wavelength decreases [35], while when using (15) it tends to zero exponentially. As our calculations show, in the region of long waves, the absorption algorithm from Ref. [35] and our algorithm have comparable efficiency.

B. The case of velocity gauge

When solving strong-field physics problems, TDSE can be written in the LG [Eq. (5)] or the VG; the following formula gives the transformation from the LG wave function to the VG:

$$\psi_V(x, t) = \psi(x, t)\exp\left(-iA(t)x + \frac{i}{2}\int_{-\infty}^{t}A^2(t')dt'\right), \tag{19}$$

where $A(t) = -\int_{-\infty}^{t}E(t')dt'$ is the projection of the vector potential onto the x axis. As a result, the TDSE is written as

$$i\frac{\partial\psi_V}{\partial t} = \left(\frac{\hat{p}^2}{2} + A(t)\hat{p}\right)\psi_V + V_c(x)\psi_V + \hat{\tilde{V}}_{\rm abs}\psi_V. \tag{20}$$

The absorbing operator $\hat{\tilde{V}}_{\rm abs}$ is given by the formulas (4) or (16) with the replacement of all partial derivatives of the wave function by

$$\frac{\partial \psi_V}{\partial x} \to \left(\frac{\partial}{\partial x} + iA(t)\right)\psi_V. \tag{21}$$

For the case when the TDSE is solved by the Fourier split-step method, the total propagator by time step $\Delta t_{\rm abs} = n\Delta t$, where Δt is the time step in the Hamiltonian propagator, is given by (18) with

$$\hat{U}_j\psi = e^{-iV_c(x)\Delta t/2}\hat{\mathcal{F}}^{-1}[e^{-i[p^2/2+A(\bar{t}_j)p]\Delta t}\hat{\mathcal{F}}[e^{-iV_c(x)\Delta t/2}\psi]],$$

which propagates the wave function from $t + (j-1)\Delta t$ to $t + j\Delta t$, $\bar{t}_j = t + (j-1/2)\Delta t$. The absorbing propagator is

$$\hat{U}_{\rm abs}\psi = \psi + \hat{\mathcal{F}}^{-1}[B_1(p)\hat{\mathcal{F}}[f\psi]], \tag{22}$$

$$B_1(p) = e^{-(C/l^2+D[p+A(t_a)]^2)\Delta t_{\rm abs}} - 1, \tag{23}$$

where $t_a = t + \Delta t_{\rm abs}/2$. Note that the absorbing propagator $\hat{U}_{\rm abs}$ is time dependent in contrast to the case of LG. Therefore, the time step $\Delta t_{\rm abs}$ must be much smaller than the vector potential oscillations time scale, which may be essential for the case of a high-frequency driving field.

C. The multidimensional case

The generalization of the proposed method to the case of several dimensions is straightforward: the corresponding absorbing operator represents the sum of operators located near different computational domain boundaries and acts in mutually orthogonal directions. Let us consider the 3D TDSE written in the Cartesian coordinates (x, y, z) in the LG for the electron wave function in the time-dependent potential $V(\mathbf{r}, t)$:

$$i\frac{\partial \psi}{\partial t} = \hat{H}\psi + \hat{V}_{\rm 3D,abs}\psi, \quad \hat{H} = \frac{\hat{\mathbf{p}}^2}{2} + V(\mathbf{r}, t), \tag{24}$$

$$\hat{\mathbf{p}}^2 = \sum_\alpha \hat{p}_\alpha^2, \quad \hat{p}_\alpha = -i\frac{\partial}{\partial \alpha}, \quad \alpha = x, y, z. \tag{25}$$

The total absorbing operator represents the sum of the operators that absorb the waves propagating along orthogonal directions:

$$\hat{V}_{\rm 3D,abs} = \sum_\alpha \hat{V}_{{\rm abs},\alpha}. \tag{26}$$

Let us suppose that the 3D TDSE (24) is solved by the Fourier split-step method in the computational domain $x_{\min} \leqslant x \leqslant x_{\max}$, $y_{\min} \leqslant y \leqslant y_{\max}$, $z_{\min} \leqslant z \leqslant z_{\max}$. To obtain high performance, the absorbing operator is set in the form (16)

$$\hat{V}_{{\rm abs},\alpha}\psi = -i\left(\frac{C}{l_\alpha^2} + D\hat{p}_\alpha^2\right)[F_\alpha(\alpha)\psi],$$

$$F_\alpha(\alpha) = f[(\alpha - \alpha_{\min} - l_\alpha)/l_\alpha] + f[(\alpha - \alpha_{\max} + l_\alpha)/l_\alpha].$$

Here, l_α is the width of the envelope of the absorbing operator acting along α coordinate; the resulting absorbing layer width is, approximately, $l_{{\rm abs},\alpha} = 2l_\alpha$. The corresponding total propagator of the wave function by step $\Delta t_{\rm abs}$ is

$$\psi(\mathbf{r}, t + \Delta t_{\rm abs}) = \hat{U}_{\rm abs}\left[\mathcal{T}\left(\prod_{j=1}^{n}\hat{U}_j\right)\psi(\mathbf{r}, t)\right]. \tag{27}$$

Here, $\hat{U}_j$ propagates the wave function under action of the Hamiltonian from $t + (j-1)\Delta t$ to $t + j\Delta t$,

$$\hat{U}_j = e^{-iV(\mathbf{r},\bar{t}_j)\Delta t/2}\hat{\mathcal{F}}_{3D}^{-1}[e^{-i\mathbf{p}^2\Delta t/2}\hat{\mathcal{F}}_{3D}[e^{-iV(\mathbf{r},\bar{t}_j)\Delta t/2}\psi]], \tag{28}$$

where $\hat{\mathcal{F}}_{3D}[\cdot]$ and $\hat{\mathcal{F}}_{3D}^{-1}[\cdot]$ are forward and backward 3D Fourier transforms, $\bar{t}_j = t + (j-1/2)\Delta t$, $\mathbf{p}^2 = \sum p_\alpha^2$, p_α is projection of the momentum $\mathbf{p}$ on the α axis, and propagator $\hat{U}_{\rm abs}$ absorbs the wave function every nth step:

$$\hat{U}_{\rm abs} = \prod_\alpha \hat{U}_{{\rm abs},\alpha}, \tag{29}$$

$$\hat{U}_{{\rm abs},\alpha}\psi = \psi + \hat{\mathcal{F}}^{-1}[B_\alpha(p_\alpha)\hat{\mathcal{F}}[F_\alpha\psi]], \tag{30}$$

$$B_\alpha(p_\alpha) = e^{-(C/l^2+Dp_\alpha^2)\Delta t_{\rm abs}} - 1, \quad \Delta t_{\rm abs} = n\Delta t. \tag{31}$$

III. THE USE OF THE ABSORBING DIFFERENTIAL OPERATOR IN STRONG-FIELD PHYSICS PROBLEMS

A. Calculations of HHG spectra in a two-color IR and XUV pulse

High-order harmonic generation is one of the main problems of strong-field physics. The numerical simulation of HHG is based on the calculation of the electron acceleration $\mathbf{a}(t) = -\langle\psi|\nabla V(\mathbf{r}, t)|\psi\rangle$, which determines the generated electromagnetic radiation [33]. Let us test the proposed absorption method when calculating the electron acceleration Fourier spectrum (HHG spectrum) for a hydrogen atom in an external two-color IR and XUV field. As is known from previous works [38–41], in such a field, HHG spectrum contains the infinite number of additional plateaus with widths equal to XUV field frequency $\omega_{\rm XUV}$. The physical reason for the additional plateaus is associated with the absorption of XUV-field photons at the electron recombination stage. Calculating the HHG spectrum beyond the main plateau cutoff requires efficient absorption of wave packets at the boundaries of the computational domain to minimize artifact wave packets that appear at the boundaries and the corresponding noise signal in the spectrum. In particular, the more efficient the absorption, the greater the number of additional plateaus visible in the spectrum.

We consider the linearly polarized field

$$\mathbf{E}(t) = \hat{\mathbf{x}}E(t), \quad E(t) = E_{\rm IR}(t) + E_{\rm XUV}(t), \tag{32}$$

$$E_\alpha(t) = \mathcal{E}_\alpha g(t)\cos(\omega_\alpha t + \varphi_\alpha), \quad \alpha = {\rm IR, XUV}, \tag{33}$$

where the envelope has the intensity full width at half maximum (FWHM) duration $\tau_p = 10$ fs and Gaussian shape $g(t) = e^{-(2\ln 2)t^2/\tau_p^2}$. The wavelengths $\lambda_\alpha = 2\pi c/\omega_\alpha$ (where c is the speed of light) of IR and XUV components are, respectively, $\lambda_{\rm IR} = 800$ nm and $\lambda_{\rm XUV} = 40$ nm. The intensities of the IR and XUV components $I_\alpha = I_a\mathcal{E}_\alpha^2/E_a^2$ (where I_a and E_a are the atomic intensity and field) are equal to $I_{\rm IR} = 1.2 \times 10^{14}$ W/cm^2 and $I_{\rm XUV} = 2 \times 10^{13}$ W/cm^2, respectively. The carrier-envelope phases are $\varphi_\alpha = 0$.

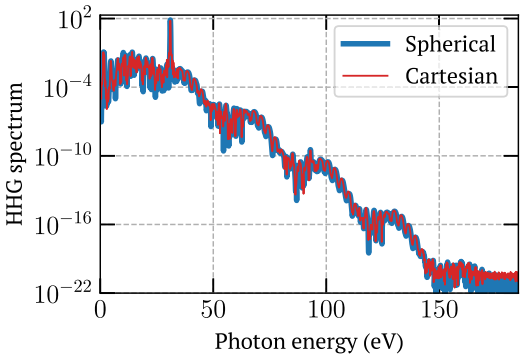

FIG. 2. The HHG spectrum obtained by solving the 3D TDSE for the H atom in the Cartesian coordinates by the Fourier split-step method using propagator (27) (thin red line). The thick blue line denotes the reference HHG spectrum obtained by solving the 3D TDSE in spherical coordinates. The calculations were performed for the two-color laser pulse with the central wavelengths of components 800 nm and 40 nm with 10 fs FWHM duration and peak intensities 1.2×10^{14} W/cm^2 and 2×10^{13} W/cm^2, respectively.

We solve the 3D TDSE (24) with the potential $V(\mathbf{r}, t) = xE(t) + V_c(r)$, where $V_c(r)$ is the smoothed Coulomb ion potential [36]:

$$V_c(r) = -\frac{1}{r}\left[\tanh\left(\frac{r}{a}\right) + \frac{r}{b}\mathrm{sech}^2\left(\frac{r}{a}\right)\right], \quad a = 0.3, \quad b = 0.46.$$

The initial condition corresponds to the ground state in the hydrogen atom. The 3D TDSE is solved numerically using the Fourier split-step method according to Sec. II C. The time step is $\Delta t = 0.02$, spatial steps are $\Delta x = \Delta y = \Delta z = 0.4$, and the numbers of grid nodes are $N_x = 512$ and $N_y = N_z = 256$. We use the following widths of envelopes of the absorbing operators acting along x, y, z: $l_x = 15$, $l_y = l_z = 7.5$ (i.e., the widths of absorbing layers are 30 along x and 15 along y and z). The resulting calculation domain covers four oscillatory radii in the IR field in the longitudinal direction. The shape of the absorbing differential operator's envelope and coefficients C and D are the same as in Sec. II. The action of absorbing operators is taken into account numerically with propagator (29) applied every $n = 5$ time steps Δt. The results of calculations of the HHG spectrum are compared in Fig. 2 with the reference spectrum from the 3D TDSE solution in a spherical coordinate system with the size of computational grid many times greater than the oscillatory radius in the IR field. A method for solving 3D TDSE in spherical coordinates is described in Appendix B. As can be seen from Fig. 2, the HHG spectra coincide with all small-scale oscillations at all frequencies, including those at low-order harmonic range and above the IR-induced cutoff at $\omega \approx 40$ eV. For both calculations, the difference in the noise level relative to the level of the main plateau in the HHG spectrum is 19 orders of magnitude. As a result, four XUV-induced plateaus are distinguished in the HHG spectrum in the region beyond the main plateau cutoff. Note that such a small noise level was obtained using rather narrow absorbing layers. Thus, the proposed absorption method is suitable for studying the harmonics with a very small yield.

B. Calculations of photoelectron momentum distributions

Above-threshold ionization is another strong-field physics phenomenon actively studied by solving the TDSE. Here, we demonstrate the capability of the absorbing differential operator as applied to calculations of PMD in an intense IR pulse. We solve the TDSE (24) for a hydrogen atom in Cartesian coordinates numerically for the linearly polarized IR field given by (32) with $\lambda_{\mathrm{IR}} = 800$ nm, $I_{\mathrm{IR}} = 1.2 \times 10^{14}$ W/cm^2, $\varphi_{\mathrm{IR}} = \pi/4$, and $I_{\mathrm{XUV}} = 0$. In this example, we set $g(t) = \cos^2(\pi t/2T_m)$ for $|t| < T_m = \pi\tau_p/[4\arccos(2^{-1/4})]$ and $g(t) = 0$ for $|t| > T_m$, where $\tau_p = 2.67$ fs is the intensity FWHM duration. The initial condition corresponds to the ground state in the atom. We define PMD as the square of the projection of the wave function onto plane waves at the time $t_{\mathrm{fin}} = T_m + 200$ (after the end of the laser field),

$$P(\mathbf{p}) = |\Psi(\mathbf{p})|^2, \quad \Psi(\mathbf{p}) = \int \psi_{\mathrm{free}}(\mathbf{r}) e^{-i\mathbf{pr}} d^3r, \tag{34}$$

where $\psi_{\mathrm{free}}(\mathbf{r})$ is the wave function in the continuum after the passage of the laser pulse. Assuming that the absorbing layer is sufficiently far from the ion and the influence of the interaction of the absorbed wave function with the ion on the PMD can be neglected, the PMD can be written using projections onto Volkov states [10,11,57,60]

$$\Psi(\mathbf{p}) = \Psi_{\mathrm{grid}}(\mathbf{p}) + \int_{-T}^{t_{\mathrm{fin}}} dt \delta\psi \exp\left(-\frac{i}{2}\int_t^{t_{\mathrm{fin}}} [\mathbf{p} + \mathbf{A}(t')]^2 dt'\right),$$

$$\delta\psi = i\int e^{-i[\mathbf{p}+\mathbf{A}(t)]\mathbf{r}} \hat{V}_{\mathrm{abs}} \psi(\mathbf{r}, t) d^3r,$$

$$\mathbf{A}(t) = \int_t^{t_{\mathrm{fin}}} \mathbf{E}(t') dt',$$

where $\hat{V}_{\mathrm{abs}}$ is the absorbing operator, $\mathbf{A}(t)$ is vector potential of the external field, and

$$\Psi_{\mathrm{grid}}(\mathbf{p}) = \int \psi(\mathbf{r}, t_{\mathrm{fin}}) M(\mathbf{r}) e^{-i\mathbf{pr}} d^3r \tag{35}$$

is the wave function of free electrons staying on the grid at the time moment t_{fin}. Here, $M(\mathbf{r})$ is the mask function that helps to filter out the most populated bound states from the full wave function $\psi(\mathbf{r}, t_{\mathrm{fin}})$ and to vanish the wave function at the boundary of the computational domain. We set the mask function as

$$M(\mathbf{r}) = M_{\mathrm{bs}}(r) M_x(x) M_y(y) M_z(z), \tag{36}$$

$$M_{\mathrm{bs}}(r) = H(r - 40, 5), \tag{37}$$

$$M_\xi(\xi) = H(\xi - \xi_{\min} - d, 7.5) H(-\xi + \xi_{\max} - d, 7.5), \tag{38}$$

$$H(\xi, s) = \frac{1}{2}\left[1 + \tanh\left(\frac{\xi}{s}\right)\right], \tag{39}$$

$$\xi = x, y, z, \quad d = 25. \tag{40}$$

Here, $H(\xi, s)$ is a smoothed step function with scale s, and $\xi_{\min}$, $\xi_{\max}$ are minimum and maximum values of the coordinate on the grid.

We use the following algorithm to calculate PMD. We solve 3D TDSE in Cartesian coordinates using the Fourier

split-step method with the time step $\Delta t = 0.02$, spatial steps $\Delta x = \Delta y = \Delta z = 0.4$, and numbers of grid nodes $N_x = 1024$, $N_y = N_z = 512$ ($x_{\max} = -x_{\min} = 204.6$, $y_{\max} = -y_{\min} = 102.2$, $z_{\max} = y_{\max}$, $z_{\min} = y_{\min}$). The absorption is performed by propagator (29) with $l_x = 50$, $l_y = l_z = 25$ every $n = 5$ steps of the main propagator (28). Every time moment when the absorption is performed, we extend the absorbed part of the wave function $\varphi = (1 - \hat{U}_{\text{abs}})\psi$ beyond the computational domain by filling with zero values; the resulting wave function array has sizes $\tilde{N}_x = 2048$, $\tilde{N}_y = 1024$, and $\tilde{N}_z = 512$ along x, y, and z, respectively. Then we make the phase shift of φ, calculate the forward 3D FFT of the resulting array, and add it to the momentum-space wave function $\Psi(\mathbf{p})$:

$$\Psi(\mathbf{p}) \to \Psi(\mathbf{p}) + e^{-(i/2)\int_t^{t_{\text{fin}}} [\mathbf{p}+\mathbf{A}(t')]^2 dt'} \hat{\mathcal{F}}_{3\text{D}}[e^{-i\mathbf{A}(t)\mathbf{r}}\varphi(\mathbf{r}, t)].$$

At the final time moment t_{fin}, the wave function remaining on the grid $\psi(\mathbf{r}, t_{\text{fin}})$ is multiplied by $M(\mathbf{r})$, extended beyond the computational domain, projected onto plane waves, and added to $\Psi(\mathbf{p})$:

$$\Psi(\mathbf{p}) \to \Psi(\mathbf{p}) + \hat{\mathcal{F}}_{3\text{D}}[\psi(\mathbf{r}, t_{\text{fin}})M(\mathbf{r})].$$

The calculation results are compared with the reference PMD obtained as a result of the 3D TDSE solution in spherical coordinates with a large computational grid (similar to testing of the t-SURFF method of PMD calculation used in Refs. [13,23]). The used size of numerical grid $r_{\max} = 1200$ exceeds the distance over which the rescattered electrons move at the end of the laser pulse, which we estimate as $\sim T_m p_0 \sim 300$ a.u. (see Appendix B for the details of PMD calculation).

Figure 3 shows the PMD in the (p_x, p_y) plane with $p_z = 0$ calculated in (a) Cartesian coordinates and (b) spherical coordinates. Figure 3(c) shows PMD distributions along p_x for the zero transverse momentum. The PMD calculated in Cartesian coordinates is in exact agreement with the reference PMD. In particular, the hemisphere associated with rescattered electrons is exactly reproduced, despite the probability density corresponding to rescattering electrons being seven orders of magnitude lower than for direct electrons. The low-energy structures are also in exact agreement. The ratio of the noise level to the maximum in PMD for the considered parameters is ten orders of magnitude. Thus, the method for calculating PMD using the proposed absorbing operator has high accuracy and can be used even in cases where the PMD amplitude is extremely small.

Note that the expansion of the numerical grid when calculating the projection onto Volkov states is necessary to increase the momentum resolution. If no grid expansion is performed, the resulting PMD contains unphysical modulation in the form of circles (see Fig. 4), which is also seen in many published numerical results (see, e.g., Fig. 1(a) in Ref. [12] or Fig. 1 in Ref. [66]). When we use the grid expansion, this unphysical structure is absent. In this case, the momentum steps along the x, y, z directions are, respectively, $\Delta p_x = 7.7 \times 10^{-3}$, $\Delta p_y = 0.015$, and $\Delta p_z = 0.031$, in accordance with the formula $\Delta p_\alpha = 2\pi/(\tilde{N}_\alpha \Delta\alpha)$, $\alpha = x, y, z$. Such steps are sufficient to resolve oscillations in PMD for given laser-pulse parameters. We estimate the scale of oscillations as $\sim\omega_{\text{IR}}/p_0 \approx 0.03$, where $p_0 = \sqrt{20U_p}$ is the

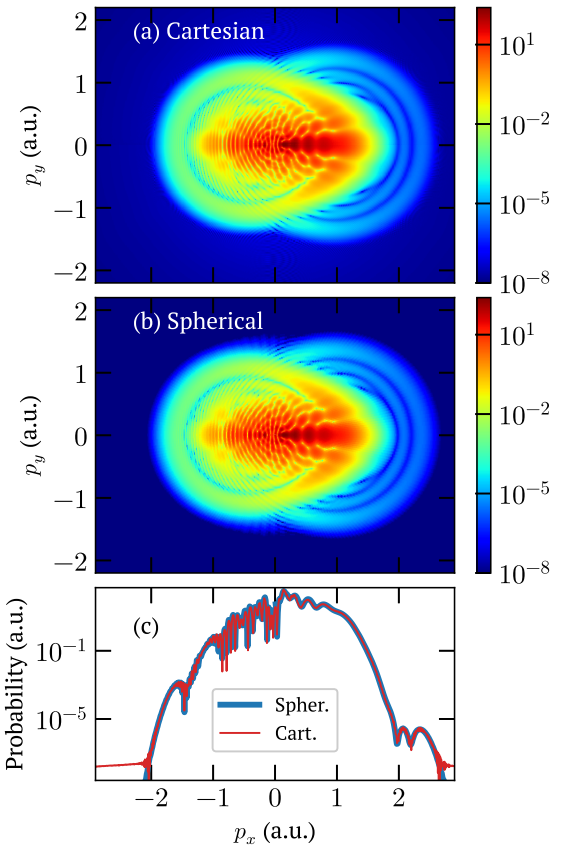

FIG. 3. Photoelectron momentum distribution in (p_x, p_y) plane for $p_z = 0$ for the H atom irradiated by linearly polarized laser pulse with wavelength 800 nm, intensity 1.2×10^{14} W/cm^2, FWHM duration $\tau_p = 2.67$ fs, and carrier-envelope phase $\varphi_{\text{IR}} = \pi/4$. (a) Calculation in the Cartesian coordinates using projections of the absorbed wave packets onto Volkov states with grid expansion to $\tilde{N}_x = 2048$, $\tilde{N}_y = 1024$, $\tilde{N}_z = 512$; (b) reference calculation in spherical coordinates with large computational grid (see text). (c) Probability density at zero transverse momentum ($p_y = p_z = 0$) as a function of p_x.

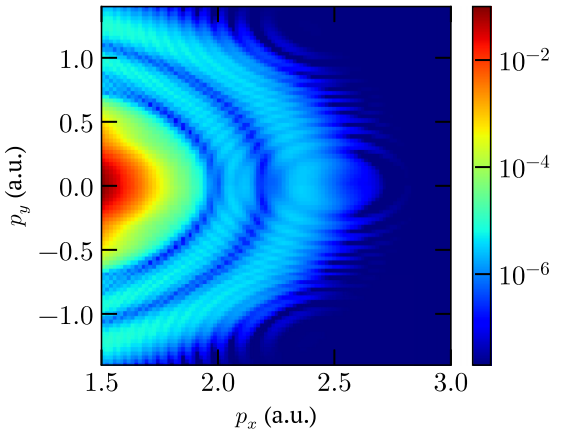

FIG. 4. The same as in Fig. 3(a), but without grid expansion to calculate the projections of the wave function onto Volkov states (see text).

maximum momentum gained by rescattered wave packets and $U_p = \mathcal{E}_{\rm IR}^2/4\omega_{\rm IR}^2$. Thus, the steps in the resulting momentum distribution in the (p_x, p_y) are much smaller than the oscillations period, in contrast to the case when no grid expansion is performed. Since projections are calculated once per $n \gg 1$ steps of the Hamiltonian propagator, the proposed computational grid expansion does not lead to a noticeable decrease in program performance.

IV. CONCLUSION

We have proposed the use of the absorbing second-order imaginary differential operator to prevent undesirable reflection from the boundaries or wrap-around of the wave packets when solving the TDSE. For the one-dimensional case, the absorbing operator for the LG of the electric field is given by (4), while for the VG it is given by (4) with the replacement of the derivative $\frac{\partial}{\partial x} \to \frac{\partial}{\partial x} + iA(t)$ when applied to the wave function (see Sec. II B). The generalization for the multidimensional case is straightforward: the corresponding absorbing operator represents the sum of operators acting in mutually orthogonal directions near different computational domain boundaries, and the envelopes of operators need not be identical (see Sec. II C). The operator suppresses de Broglie waves propagating towards the boundaries and away from them with equal efficiency. The survival probability decreases exponentially with decreasing wavelength. For the operator with the Gaussian envelope with a width of l, the survival of de Broglie wavelength of size $2l$ (equal to the width of the absorbing layer) is 0.01. In the wavelength range higher than $2l$, absorption efficiency is higher than that provided by a bell-shaped imaginary potential having optimal amplitude for a given wavelength.

Operator (4) can be directly used to solve TDSE by finite difference methods and does not affect the performance of calculations since the numerical approximation of the absorbing operator is similar to the approximation of the kinetic energy operator. In particular, this operator can be implemented when solving 3D TDSE or TDKSE using high-order finite difference methods in Cartesian coordinates [58,59] or the expansion in terms of spherical harmonics and solution of the system of 1D TDSE for the radial wave functions [21,46,54,56,65]. When using the Fourier split-step method [25,57,66], implementation of operator (4) can be provided by the propagator (13), (14) but needs a small time step to ensure the stability of the numerical scheme. In this regard, we proposed to specify the absorbing operator in a slightly modified form (16); the corresponding propagator for the LG is given by (13), (15), and for the VG, as (22), (23) and is stable at an arbitrarily large time step, which can be much higher than the time step in the propagator of the Hamiltonian. Thus, the absorption propagator can be applied at every nth step of the main propagator, and for $n \gg 1$, there is no reduction in computer code performance. For the modified absorbing operator (16), the absorption efficiency is slightly decreased compared to the original operator in the narrow range of the de Broule wavelengths $\sim$3–10l, and the resulting absorption efficiency is similar to the case of the single-hump imaginary potential with optimal amplitude for a given wavelength.

We expect that implementation of the proposed absorption method in known open-source codes [19,23,55–59] can significantly increase the accuracy of calculations, in particular, reduce the noise level in HHG spectra and PMDs and remove the unphysical oscillations in the low-energy part of PMDs when using t-SURFF [19,23]. We have demonstrated that the use of the proposed absorption method based on propagator (27), (29) for solving 3D TDSE in Cartesian coordinates allows obtaining record low noise level in the electron acceleration spectrum ($\sim$19 order of magnitude smaller than the plateau intensity), which is important for many problems, such as the study of HHG in IR and XUV pulses [37–41]. We have also demonstrated the convenience and high accuracy of using the proposed absorption method for calculating PMDs based on projecting the absorbed part of the wave function onto Volkov states. Finally, we have shown that the expansion of the spatial grid before calculating the projections on Volkov states can eliminate the unphysical circles structure in PMDs associated with insufficient momentum resolution.

ACKNOWLEDGMENTS

The numerical calculations were supported by the Russian Science Foundation through Grant No. 22-72-10133. A.A.S. acknowledges the Foundation for the Advancement of Theoretical Physics and Mathematics "BASIS" (22-1-3-51-1) for financial support.

APPENDIX A: NUMERICAL SOLUTION OF 1D SSE

To solve SSE (1) or (7) with boundary conditions (2) we make a change of variables $\eta = -x/l$, $\psi(x) = \tilde{\psi}(\eta)$, $\kappa = kl$ and solve the dimensionless SSE

$$-\frac{1}{2}\frac{d^2\tilde{\psi}}{d\eta^2} + \hat{v}_{\rm abs}\tilde{\psi} = \frac{\kappa^2}{2}\tilde{\psi} \tag{A1}$$

with boundary conditions

$$\tilde{\psi} = \begin{cases} \tilde{t}^{-1}e^{-i\kappa\eta} + \tilde{r}\tilde{t}^{-1}e^{i\kappa\eta}, & \eta \to \infty, \\ e^{-i\kappa\eta}, & \eta \to -\infty. \end{cases} \tag{A2}$$

The operator

$$\hat{v}_{\rm abs}\tilde{\psi} = -i\varepsilon f(\eta)\tilde{\psi}, \quad \varepsilon = ul^2 \tag{A3}$$

corresponds to SSE (1) with imaginary potential (3),

$$\hat{v}_{\rm abs}\tilde{\psi} = -iCf(\eta)\tilde{\psi} + iD\frac{d}{d\eta}\left(f(\eta)\frac{d\tilde{\psi}}{d\eta}\right) \tag{A4}$$

corresponds to SSE (7) with absorbing operator (4), and

$$\hat{v}_{\rm abs}\tilde{\psi} = -i\left(C - D\frac{d^2}{d\eta^2}\right)[f(\eta)\tilde{\psi}] \tag{A5}$$

corresponds to SSE (7) with absorbing operator (16). By making a replacement $\tilde{\psi} = e^{-i\kappa\eta}\varphi$ introducing the notation $q(\eta) = d\varphi/d\eta$ we obtain the system of first-order ordinary equations

$$\begin{cases} \varphi'(\eta) = q, \\ q'(\eta) = 2i\kappa q + F(q, \varphi, \eta) \end{cases} \tag{A6}$$

with asymptotics $\varphi = 1$, $q = 0$ at $\eta \to -\infty$; for $\eta \to \infty$,

$$\tilde{t} = (\varphi - q/2i\kappa)^{-1}, \quad \tilde{r} = q\tilde{t}e^{-2i\kappa\eta}/2i\kappa. \tag{A7}$$

For the case when $\hat{v}_{\rm abs}$ is given by (A3),

$$F(q, \varphi, \eta) = 2Q(\eta)\varphi, \tag{A8}$$

for (A4),

$$F(q, \varphi, \eta) = \frac{Q(\eta)\varphi + iDf'(\eta)(q - i\kappa\varphi)}{1/2 - iDf(\eta)}, \tag{A9}$$

and for (A5),

$$F(q, \varphi, \eta) = \frac{Q(\eta)\varphi + 2iDf'(\eta)(q - i\kappa\varphi) + iDf''(\eta)\varphi}{1/2 - iDf(\eta)}, \tag{A10}$$

where $Q(\eta) = -if(\eta)(C + D\kappa^2)$. The equations (A6) are integrated by the fourth-order Runge-Kutta method with the step $\Delta\eta = 10^{-3}\min(\nu, 1)$, where $\nu = 2\pi/\kappa$, with initial conditions $\varphi = 1$, $q = 0$ at $\eta = -\eta_0$, where $\eta_0 = 3 + 2\nu$. The coefficients $\tilde{t}$ and $\tilde{r}$ are found at $\eta = \eta_0$.

APPENDIX B: ALGORITHM FOR THE 3D TDSE SOLUTION IN SPHERICAL COORDINATES

To solve the 3D TDSE in the spherical system of coordinates (r, θ, ϕ), the wave function is decomposed into spherical harmonics [46]

$$\psi(r, \theta, \phi, t) = \frac{1}{r}\sum_{l=0}^{\infty} \Phi_l(r, t)Y_{l0}(\theta, \phi), \tag{B1}$$

where $Y_{l0}(\theta, \phi) = [(2l + 1)/4\pi]^{1/2}P_l(\cos\theta)$, l is angular momentum, $P_l(\cos\theta)$ are Legendre polynomials, and θ, ϕ are the polar and azimuthal spherical angles, respectively, corresponding to the polar axis x. Due to the cylindrical symmetry of the problem and initial $1s$ state, the magnetic quantum number is restricted to zero. Substituting (B1) in the TDSE, we obtain a system of equations for Φ_l,

$$i\frac{\partial\Phi_l}{\partial t} = \left[-\frac{1}{2}\frac{\partial^2}{\partial r^2} + \frac{l(l+1)}{2r^2} + V_c(r) + U_{\rm CAP}(r)\right]\Phi_l + rE(t)(c_{l-1}\Phi_{l-1} + c_l\Phi_{l+1}), \tag{B2}$$

where $c_l = (l + 1)[(2l + 1)(2l + 3)]^{-1/2}$. The electron acceleration $\mathbf{a}(t) = \hat{\mathbf{x}}a(t)$ is found as

$$a(t) = -E(t) - 2\sum_{l=0}^{\infty} c_l {\rm Re}\left[\int_0^{\infty} dr\Phi_l^*\Phi_{l+1}(\partial V_c/\partial r)\right].$$

The system of equations (B2) is solved using the finite difference discretization of the radial coordinate with the Numerov approximation for the second derivative [54]. The calculation is carried out in the region $-2\tau_p \leqslant t \leqslant 2\tau_p$ for Fig. 2 and $-T_m \leqslant t \leqslant T_m + 200$ for Fig. 3, $0 \leqslant l \leqslant L_{\rm max}$, $L_{\rm max} = 512$, $0 \leqslant r \leqslant r_{\rm max}$, where $r_{\rm max} = 300$ for Fig. 2 and $r_{\rm max} = 1200$ for Fig. 3. An equidistant grid with radial step $\Delta r = 0.2$ is used. The time step is $\Delta t = 0.02$. To absorb the wave function near the grid boundary, the three-hump imaginary potential $U_{\rm CAP}(r)$ of total width 100 is introduced, which provides high efficiency of absorption in a wide wavelength range. We use the algorithm presented in Ref. [65] to set the parameters of imaginary potential.

Photoelectron momentum distribution is found using (34) and an analytical expansion of a plane wave in terms of spherical harmonics,

$$\exp(i\mathbf{pr}) = 4\pi\sum_{l=0}^{\infty}\sum_{m=-l}^{l} i^l j_l(pr)Y_{lm}^*(\theta, \phi)Y_{lm}(\theta_p, \phi_p), \tag{B3}$$

where angles θ_p, ϕ_p define vector $\mathbf{p}$ direction, and j_l are the spherical Bessel functions. Substituting (B1), (B3) into (34) and integrating over θ, ϕ, we obtain an expression for the projection of the wave function onto plane waves:

$$\Psi_{\rm free}(\mathbf{p}) = 4\pi\sum_{l=0}^{\infty}(-i)^l Y_{l0}(\theta_p, \phi_p) \times \int_0^{\infty}\Phi_l(r, t_{\rm fin})M_{\rm bs}(r)j_l(pr)rdr.$$

Here, $t_{\rm fin}$ is the final time moment and the mask function $M_{\rm bs}(r)$ [given by (37)] serves to exclude populated bound states.

[1] C. W. McCurdy, C. K. Stroud, and M. K. Wisinski, Solving the time-dependent Schrödinger equation using complex-coordinate contours, Phys. Rev. A **43**, 5980 (1991).

[2] J. L. Krause, K. J. Schafer, and K. C. Kulander, Calculation of photoemission from atoms subject to intense laser fields, Phys. Rev. A **45**, 4998 (1992).

[3] A. Scrinzi, Infinite-range exterior complex scaling as a perfect absorber in time-dependent problems, Phys. Rev. A **81**, 053845 (2010).

[4] D. A. Telnov, K. E. Sosnova, E. Rozenbaum, and S.-I. Chu, Exterior complex scaling method in time-dependent density-functional theory: Multiphoton ionization and high-order-harmonic generation of Ar atoms, Phys. Rev. A **87**, 053406 (2013).

[5] T. Hagstrom, New results on absorbing layers and radiation boundary conditions, in *Topics in Computational Wave Propagation*, edited by M. Ainsworth, P. Davies, D. Duncan, B. Rynne, and P. Martin (Springer, Berlin, Heidelberg, 2003), pp. 1–42.

[6] J. G. Muga, J. P. Palao, B. Navarro, and I. L. Egusquiza, Complex absorbing potentials, Phys. Rep. **395**, 357 (2004).

[7] J. P. Boyd, *Chebyshev and Fourier Spectral Methods* (Courier Corporation, 2001).

[8] W. H. Press, S. A. Teukolsky, W. T. Vetterling, and B. P. Flannery, *Numerical Recipes: The Art of Scientific Computing*, 3rd ed. (Cambridge University Press, New York, 2007).

[9] H. C. Kamban, S. S. Christensen, T. Søndergaard, and T. G. Pedersen, Finite-difference time-domain simulation of

strong-field ionization: A perfectly matched layer approach, Phys. Status Solidi (B) **257**, 1900467 (2020).
[10] D. B. Milošević, G. G. Paulus, D. Bauer, and W. Becker, Above-threshold ionization by few-cycle pulses, J. Phys. B: At. Mol. Opt. Phys. **39**, R203 (2006).
[11] M. V. Frolov, D. V. Knyazeva, N. L. Manakov, A. M. Popov, O. V. Tikhonova, E. A. Volkova, M.-H. Xu, L.-Y. Peng, L.-W. Pi, and A. F. Starace, Validity of Factorization of the High-Energy Photoelectron Yield in Above-Threshold Ionization of an Atom by a Short Laser Pulse, Phys. Rev. Lett. **108**, 213002 (2012).
[12] J. Henkel and M. Lein, Analysis of electron trajectories with two-color strong-field ionization, Phys. Rev. A **92**, 013422 (2015).
[13] B. Fetić, M. Tunja, W. Becker, and D. B. Milošević, Extracting photoelectron spectra from the time-dependent wave function. II. Validation of two methods: Projection on plane waves and time-dependent surface flux, Phys. Rev. A **105**, 053121 (2022).
[14] A. V. Sviridov, M. V. Frolov, S. V. Popruzhenko, L. Geng, and L.-Y. Peng, Coulomb effects in the high-energy part of above-threshold-ionization spectra in intense bicircular laser fields, Phys. Rev. A **106**, 033117 (2022).
[15] T.-M. Yan, S. V. Popruzhenko, M. J. J. Vrakking, and D. Bauer, Low-Energy Structures in Strong Field Ionization Revealed by Quantum Orbits, Phys. Rev. Lett. **105**, 253002 (2010).
[16] B. Wolter, C. Lemell, M. Baudisch, M. G. Pullen, X.-M. Tong, M. Hemmer, A. Senftleben, C. D. Schröter, J. Ullrich, R. Moshammer, J. Biegert, and J. Burgdörfer, Formation of very-low-energy states crossing the ionization threshold of argon atoms in strong mid-infrared fields, Phys. Rev. A **90**, 063424 (2014).
[17] N. I. Shvetsov-Shilovski, M. Lein, and L. B. Madsen, Multielectron polarization effects in strong-field ionization: Narrowing of momentum distributions and imprints in interference structures, Phys. Rev. A **98**, 023406 (2018).
[18] D. B. Milošević and W. Becker, Atom-Volkov strong-field approximation for above-threshold ionization, Phys. Rev. A **99**, 043411 (2019).
[19] V. Tulsky and D. Bauer, QPROP with faster calculation of photoelectron spectra, Comput. Phys. Commun. **251**, 107098 (2020).
[20] L. Tao and A. Scrinzi, Photo-electron momentum spectra from minimal volumes: The time-dependent surface flux method, New J. Phys. **14**, 013021 (2012).
[21] F. Morales, T. Bredtmann, and S. Patchkovskii, iSURF: A family of infinite-time surface flux methods, J. Phys. B: At. Mol. Opt. Phys. **49**, 245001 (2016).
[22] A. Scrinzi, tRecX–An environment for solving time-dependent Schrödinger-like problems, Comput. Phys. Commun. **270**, 108146 (2022).
[23] Z.-H. Zhang, Y. Li, Y.-J. Mao, and F. He, QPC-TDSE: A parallel TDSE solver for atoms and small molecules in strong lasers, Comput. Phys. Commun. **290**, 108787 (2023).
[24] A. A. Silaev and N. V. Vvedenskii, Residual-Current Excitation in Plasmas Produced by Few-Cycle Laser Pulses, Phys. Rev. Lett. **102**, 115005 (2009).
[25] A. A. Silaev, M. Y. Ryabikin, and N. V. Vvedenskii, Strong-field phenomena caused by ultrashort laser pulses: Effective one- and two-dimensional quantum-mechanical descriptions, Phys. Rev. A **82**, 033416 (2010).
[26] L. N. Alexandrov, M. Y. Emelin, and M. Y. Ryabikin, Unidirectional current excitation in tunneling ionization of asymmetric molecules, Phys. Rev. A **87**, 013414 (2013).
[27] W. B. Chen, Y. D. Huang, C. Meng, J. L. Liu, Z. Y. Zhou, D. W. Zhang, J. M. Yuan, and Z. X. Zhao, Theoretical study of terahertz generation from atoms and aligned molecules driven by two-color laser fields, Phys. Rev. A **92**, 033410 (2015).
[28] A. A. Silaev and N. V. Vvedenskii, Analytical description of generation of the residual current density in the plasma produced by a few-cycle laser pulse, Phys. Plasmas **22**, 053103 (2015).
[29] V. A. Kostin, I. D. Laryushin, A. A. Silaev, and N. V. Vvedenskii, Ionization-Induced Multiwave Mixing: Terahertz Generation with Two-Color Laser Pulses of Various Frequency Ratios, Phys. Rev. Lett. **117**, 035003 (2016).
[30] A. A. Silaev, A. A. Romanov, and N. V. Vvedenskii, Generation of tunable mid-and far-infrared pulses during gas ionization by a chirped two-color laser field, Opt. Lett. **45**, 4527 (2020).
[31] A. A. Silaev, V. A. Kostin, I. D. Laryushin, and N. V. Vvedenskii, Ionization mechanism of the generation of tunable ultrashort pulses in the mid-infrared range, JETP Lett. **107**, 151 (2018).
[32] Z. Zhou, D. Zhang, J. Liu, Z. Zhao, and C. D. Lin, Searching for optimal THz generation through calculations of the asymmetry of photoelectron momentum distributions by an improved strong-field-approximation method, Phys. Rev. A **107**, 013106 (2023).
[33] P. B. Corkum, Plasma Perspective on Strong Field Multiphoton Ionization, Phys. Rev. Lett. **71**, 1994 (1993).
[34] F. Krausz and M. Ivanov, Attosecond physics, Rev. Mod. Phys. **81**, 163 (2009).
[35] V. V. Strelkov, M. A. Khokhlova, A. A. Gonoskov, I. A. Gonoskov, and M. Y. Ryabikin, High-order harmonic generation by atoms in an elliptically polarized laser field: Harmonic polarization properties and laser threshold ellipticity, Phys. Rev. A **86**, 013404 (2012).
[36] M. V. Frolov, N. L. Manakov, A. A. Minina, N. V. Vvedenskii, A. A. Silaev, M. Y. Ivanov, and A. F. Starace, Control of Harmonic Generation by the Time Delay Between Two-Color, Bicircular Few-Cycle Mid-IR Laser Pulses, Phys. Rev. Lett. **120**, 263203 (2018).
[37] A. C. Brown and H. W. Van Der Hart, Extreme-Ultraviolet-Initated High-Order Harmonic Generation: Driving Inner-Valence Electrons Using Below-Threshold-Energy Extreme-Ultraviolet Light, Phys. Rev. Lett. **117**, 093201 (2016).
[38] T. S. Sarantseva, M. V. Frolov, N. L. Manakov, A. A. Silaev, N. V. Vvedenskii, and A. F. Starace, XUV-assisted high-order-harmonic-generation spectroscopy, Phys. Rev. A **98**, 063433 (2018).
[39] T. S. Sarantseva, M. V. Frolov, N. L. Manakov, A. A. Silaev, A. A. Romanov, N. V. Vvedenskii, and A. F. Starace, Attosecond-pulse metrology based on high-order harmonic generation, Phys. Rev. A **101**, 013402 (2020).
[40] T. S. Sarantseva, A. A. Silaev, A. A. Romanov, N. V. Vvedenskii, and M. V. Frolov, Time-frequency analysis of high harmonic generation using a probe XUV pulse, Opt. Express **29**, 1428 (2021).
[41] T. S. Sarantseva, A. A. Romanov, A. A. Silaev, N. V. Vvedenskii, and M. V. Frolov, Waveform retrieving of an isolated attosecond pulse using high-order harmonics generation

of the superimposed infrared field, Opt. Express **29**, 38298 (2021).

[42] U. De Giovannini, A. H. Larsen, and A. Rubio, Modeling electron dynamics coupled to continuum states in finite volumes with absorbing boundaries, Eur. Phys. J. B **88**, 56 (2015).

[43] C. Leforestier, R. Bisseling, C. Cerjan, M. Feit, R. Friesner, A. Guldberg, A. Hammerich, G. Jolicard, W. Karrlein, H.-D. Meyer, N. Lipkin, O. Roncero, and R. Kosloff, A comparison of different propagation schemes for the time dependent Schrödinger equation, J. Comput. Phys. **94**, 59 (1991).

[44] A. Nissen and G. Kreiss, An optimized perfectly matched layer for the Schrödinger equation, Commun. Comput. Phys. **9**, 147 (2011).

[45] J. Caillat, J. Zanghellini, M. Kitzler, O. Koch, W. Kreuzer, and A. Scrinzi, Correlated multielectron systems in strong laser fields: A multiconfiguration time-dependent Hartree-Fock approach, Phys. Rev. A **71**, 012712 (2005).

[46] A. D. Bandrauk, S. Chelkowski, D. J. Diestler, J. Manz, and K.-J. Yuan, Quantum simulation of high-order harmonic spectra of the hydrogen atom, Phys. Rev. A **79**, 023403 (2009).

[47] A. Crawford-Uranga, U. De Giovannini, E. Räsänen, M. J. T. Oliveira, D. J. Mowbray, G. M. Nikolopoulos, E. T. Karamatskos, D. Markellos, P. Lambropoulos, S. Kurth, and A. Rubio, Time-dependent density-functional theory of strong-field ionization of atoms by soft x rays, Phys. Rev. A **90**, 033412 (2014).

[48] M. Murakami, G. P. Zhang, and S.-I. Chu, Multielectron effects in the photoelectron momentum distribution of noble-gas atoms driven by visible-to-infrared-frequency laser pulses: A time-dependent density-functional-theory approach, Phys. Rev. A **95**, 053419 (2017).

[49] A. A. Romanov, A. A. Silaev, M. V. Frolov, and N. V. Vvedenskii, Influence of the polarization of a multielectron atom in a strong laser field on high-order harmonic generation, Phys. Rev. A **101**, 013435 (2020).

[50] O. Neufeld and O. Cohen, Probing ultrafast electron correlations in high harmonic generation, Phys. Rev. Res. **2**, 033037 (2020).

[51] A. A. Romanov, A. A. Silaev, T. S. Sarantseva, M. V. Frolov, and N. V. Vvedenskii, Study of high-order harmonic generation in xenon based on time-dependent density-functional theory, New J. Phys. **23**, 043014 (2021).

[52] D. E. Manolopoulos, Derivation and reflection properties of a transmission-free absorbing potential, J. Chem. Phys. **117**, 9552 (2002).

[53] M. B. Soley, K. N. Avanaki, and E. J. Heller, Reducing anomalous reflection from complex absorbing potentials: A semiclassical approach, Phys. Rev. A **103**, L041301 (2021).

[54] D. Bauer and P. Koval, QPROP: A Schrödinger-solver for intense laser–atom interaction, Comput. Phys. Commun. **174**, 396 (2006).

[55] S. Patchkovskii and H. G. Muller, Simple, accurate, and efficient implementation of 1-electron atomic time-dependent Schrödinger equation in spherical coordinates, Comput. Phys. Commun. **199**, 153 (2016).

[56] C. Ó. Broin and L. Nikolopoulos, A GPGPU based program to solve the TDSE in intense laser fields through the finite difference approach, Comput. Phys. Commun. **185**, 1791 (2014).

[57] Y. Fu, J. Zeng, and J. Yuan, PCTDSE: A parallel Cartesian-grid-based TDSE solver for modeling laser–atom interactions, Comput. Phys. Commun. **210**, 181 (2017).

[58] A. Castro, H. Appel, M. Oliveira, C. A. Rozzi, X. Andrade, F. Lorenzen, M. A. Marques, E. Gross, and A. Rubio, Octopus: A tool for the application of time-dependent density functional theory, Phys. Status Solidi (B) **243**, 2465 (2006).

[59] X. Andrade, J. Alberdi-Rodriguez, D. A. Strubbe, M. J. T. Oliveira, F. Nogueira, A. Castro, J. Muguerza, A. Arruabarrena, S. G. Louie, A. Aspuru-Guzik, A. Rubio, and M. A. L. Marques, Time-dependent density-functional theory in massively parallel computer architectures: The OCTOPUS project, J. Phys.: Condens. Matter **24**, 233202 (2012).

[60] S. Chelkowski and A. Bandrauk, Above-threshold ionization electron spectra from a dissociating molecular ion calculated using the wave-function splitting technique, Laser Phys. **7**, 797 (1997).

[61] U. De Giovannini, D. Varsano, M. A. L. Marques, H. Appel, E. K. U. Gross, and A. Rubio, *Ab initio* angle- and energy-resolved photoelectron spectroscopy with time-dependent density-functional theory, Phys. Rev. A **85**, 062515 (2012).

[62] U. De Giovannini, G. Brunetto, A. Castro, J. Walkenhorst, and A. Rubio, Simulating pump–probe photoelectron and absorption spectroscopy on the attosecond timescale with time-dependent density functional theory, ChemPhysChem **14**, 1363 (2013).

[63] A. Crawford-Uranga, U. De Giovannini, D. J. Mowbray, S. Kurth, and A. Rubio, Modelling the effect of nuclear motion on the attosecond time-resolved photoelectron spectra of ethylene, J. Phys. B: At. Mol. Opt. Phys. **47**, 124018 (2014).

[64] Y. Yu and B. D. Esry, An optimized absorbing potential for ultrafast, strong-field problems, J. Phys. B: At. Mol. Opt. Phys. **51**, 095601 (2018).

[65] A. A. Silaev, A. A. Romanov, and N. V. Vvedenskii, Multi-hump potentials for efficient wave absorption in the numerical solution of the time-dependent Schrödinger equation, J. Phys. B: At. Mol. Opt. Phys. **51**, 065005 (2018).

[66] J.-P. Wang and F. He, Tunneling ionization of neon atoms carrying different orbital angular momenta in strong laser fields, Phys. Rev. A **95**, 043420 (2017).

[67] A. D. Bandrauk and H. Shen, Higher order exponential split operator method for solving time-dependent Schrödinger equations, Can. J. Chem. **70**, 555 (1992).

[68] I. Gonoskov and M. Marklund, Single-step propagators for calculation of time evolution in quantum systems with arbitrary interactions, Comput. Phys. Commun. **202**, 211 (2016).